










Stellar Bars in Isolated Gas-rich Spiral Galaxies Do Not Slow Down

Angus Beane¹ , Lars Hernquist¹ , Elena D’Onghia^{2,3}, Federico Marinacci⁴ , Charlie Conroy¹ , Jia Qi⁵, Laura V. Sales⁶ , Paul Torrey⁵ , and Mark Vogelsberger⁷ 

¹ Center for Astrophysics, Harvard & Smithsonian, Cambridge, MA, USA; angus.beane@cfa.harvard.edu

² Department of Physics, University of Wisconsin-Madison, Madison, WI, USA

³ Department of Astronomy, University of Wisconsin-Madison, Madison, WI, USA

⁴ Department of Physics & Astronomy “Augusto Righi,” University of Bologna, Bologna, Italy

⁵ Department of Astronomy, University of Florida, Gainesville, FL, USA

⁶ Department of Physics & Astronomy, University of California, Riverside, CA, USA

⁷ Department of Physics, Massachusetts Institute of Technology, Cambridge, MA, USA

Received 2023 January 6; revised 2023 June 12; accepted 2023 June 18; published 2023 August 16

Abstract

Elongated bar-like features are ubiquitous in galaxies, occurring at the centers of approximately two-thirds of spiral disks in the nearby Universe. Due to gravitational interactions between the bar and the other components of galaxies, it is expected that angular momentum and matter will redistribute over long (Gyr) timescales in barred galaxies. Previous work ignoring the gas phase of galaxies has conclusively demonstrated that bars should slow their rotation over time due to their interaction with dark matter halos. We have performed a simulation of a Milky Way–like galactic disk hosting a strong bar, including a state-of-the-art model of the interstellar medium and a live dark matter halo. In this simulation, the bar pattern does not slow down over time, and instead it remains at a stable, constant rate of rotation. This behavior has been observed in previous simulations using more simplified models for the interstellar gas, but the apparent lack of secular evolution has remained unexplained. We find that the presence of the gas phase arrests the process by which the dark matter halo slows down a bar, a phenomenon we term bar locking. This locking is responsible for stabilizing the bar pattern speed. We find that, in a Milky Way–like disk, a gas fraction of only about 5% is necessary for this mechanism to operate. Our result naturally explains why nearly all observed bars rotate rapidly and is especially relevant for our understanding of how the Milky Way arrived at its present state.

Unified Astronomy Thesaurus concepts: Barred spiral galaxies (136); Hydrodynamical simulations (767); Galaxy dynamics (591); Milky Way dynamics (1051); Milky Way evolution (1052); Milky Way Galaxy (1054)

1. Introduction


Approximately two-thirds of spiral disks host an elongated bar-like feature at their centers (Eskridge et al. 2000; Menéndez-Delmestre et al. 2007), including our own Milky Way (Johnson 1957; Blitz & Spergel 1991). The ubiquity of bars is not difficult to explain, since stellar disks simulated in isolation almost always form bar-like structures (Hohl 1971). Several studies have shown that a hot, centrally concentrated mass distribution, such as a stellar bulge or dark matter halo, acts to stabilize stellar disks against bar formation (e.g., Ostriker & Peebles 1973; Hohl 1976).

It is more difficult to reconcile numerical simulations with the observed pattern speeds of extragalactic bars. Currently, the best technique for measuring the pattern speeds of individual galaxies is the Tremaine–Weinberg method (Tremaine & Weinberg 1984a; Corsini 2011). This approach has recently been applied to samples of galaxies from the MaNGA survey (Guo et al. 2019; Garma-Oehmichen et al. 2020) and CALIFA survey (Aguerri et al. 2015). These studies confirm what was found in earlier works, namely that nearly all extragalactic bars are fast rotators (i.e., they rotate close to their maximum rotation rate).

This is a problem for theoretical simulations, for which there is ample evidence that galactic bars should resonantly interact

with the dark matter halo, causing the bar to slow down over time (Combes & Sanders 1981; Hernquist & Weinberg 1992; Debattista & Sellwood 2000; Athanassoula 2002, 2003; Athanassoula & Misiriotis 2002; O’Neill & Dubinski 2003; Holley-Bockelmann et al. 2005; Martínez-Valpuesta et al. 2006; Weinberg & Katz 2007; Dubinski et al. 2009). The physical mechanism of this interaction can be understood as an angular form of dynamical friction between the bar and the dark matter halo. While studied in detail for the bar (Tremaine & Weinberg 1984b; Weinberg 1985), this process is generic for any non-axisymmetric disturbance (Lynden-Bell & Kalnajs 1972). (For an old but still useful review of bar dynamics, see Sellwood & Wilkinson 1993.)

Bar pattern speeds are usually measured using the parameter $\mathcal{R} = R_{\text{CR}}/R_{\text{b}}$, where R_{CR} is the corotation radius and R_{b} is the bar length.⁸ Bars with $\mathcal{R} < 1.4$ are considered “fast rotators,” while bars with $\mathcal{R} > 1.4$ are considered “slow rotators” (Debattista & Sellwood 2000). Bars with $\mathcal{R} < 1$ are not thought to be stable (Contopoulos 1980). Observational estimates of the pattern speeds of bars indicate that nearly all galaxies have $1 < \mathcal{R} < 1.4$ (Corsini 2011; Aguerri et al. 2015; Guo et al. 2019; Garma-Oehmichen et al. 2020). We note that Font et al. (2017) argue that the pattern speed should be measured relative to a characteristic angular velocity of the outer disk.

 Original content from this work may be used under the terms of the [Creative Commons Attribution 4.0 licence](https://creativecommons.org/licenses/by/4.0/). Any further distribution of this work must maintain attribution to the author(s) and the title of the work, journal citation and DOI.

⁸ The radius of corotation R_{CR} is defined for circular orbits as the radius at which the orbital frequency is equal to the pattern speed, Ω_{p} , of a given non-axisymmetric feature. In a galaxy with a constant circular velocity V_{c} , it is given by $R_{\text{CR}} = V_{\text{c}}/\Omega_{\text{p}}$.

While the fact that a bar is slowed down by a dark matter halo is well-understood theoretically, this is not the case for the interaction between a bar and a gaseous disk. Some argue that the gas disk should slow down the bar more (Athanasoula 2003), while others argue that the tendency of the bar to drive gas inward means the bar should speed up due to the effect of the gas disk (Athanasoula et al. 2013; Athanasoula 2014). Given that the gas phase typically contributes only about 10%–20% of the mass of a galaxy at the present day, one might naively expect it to have a subdominant effect on the bar. However, because gas is collisional, it can participate in nonresonant angular momentum exchange with the bar (Hopkins & Quataert 2011). Thus, numerical work has shown that the gas phase can have a stronger influence on a bar than its contribution to the mass of a galaxy would suggest (e.g., Villa-Vargas et al. 2010; Athanasoula et al. 2013).

In the last decade, stellar bars have been studied mainly in the context of the instability processes that lead to their formation and their ability to drive gas toward the galaxy center and contribute to the formation of supermassive black holes (SMBHs). The primary interest of these studies was the loss of angular momentum of the gas and the associated gaseous flow down to the inner disk, possibly forming a central mass concentration (Villa-Vargas et al. 2010) and fueling the central SMBH (e.g., Shlosman et al. 1989, 1990). A revisit of the more general problem of galactic bar properties and formation, including the case of disk galaxies with very large gas fraction is timely because it is clear now that galactic disks show massive bars already at redshift $z > 2$ (Guo et al. 2023). At that time, the universe was 2.5 billion year old and galaxies might have gas fractions as high as 80% (Tacconi et al. 2020). Furthermore, unlike nearby disk galaxies, the high-redshift disks also continuously accrete cold gas from the cosmic web, making the formation, stability, and evolution of non-axisymmetric features a key question to address, because they can play a fundamental role in the more general problem of disk galaxy evolution.

We have performed a simulation of a disk galaxy using the finite-volume, gravito-hydrodynamics code AREPO (Springel 2010). We use the galaxy formation model Stars and MULTiphase Gas in GaLaxiEs (SMUGGLE; Marinacci et al. 2019). This disk galaxy exhibits almost no evolution in the bar pattern speed over several Gyr when the gas phase is accounted for and robustly modeled. This behavior has been observed in previous works (Friedli & Benz 1993; Berentzen et al. 2007; Villa-Vargas et al. 2009, 2010; Athanasoula 2014). We propose a new physical explanation for this stable behavior.

In particular, we find that the presence of a gas phase in a barred galaxy can arrest the process by which the dark matter halo brakes the bar. The constant positive torque on the bar by the gas causes the bar’s resonance to reside in regions that have become depopulated. In the halo wake picture, this is equivalent to no new material being available to reinforce the wake. We show that this occurs in Milky Way–like disks with gas fractions as low as about 5%.

We show stellar mass distributions of our barred galaxy in cases with and without gas in Figure 1. We see that the bar grows longer and stronger without gas (bar length shown as a white bar), while it remains at approximately the same length and strength when gas is included. As the bar without gas slows

down, the corotation radius (white dashed circle) grows larger with time.

In Section 2, we describe our initial setup, numerical model, and details on our bar analysis procedures. In Section 3, we summarize the main results from our findings. We discuss these findings at more length and in the context of previous research in Section 4 before concluding in Section 5.

2. Methods

2.1. Initial Conditions

The initial setup of the galactic disk used in this work closely follows the GALAKOS model (D’Onghia & Aguerrí 2020), which uses a modified version of the `MakeNewDisk` code (Springel et al. 2005). The GALAKOS model has three components: a radially exponential and vertically isothermal stellar disk, a stellar bulge, and a dark matter halo following a Hernquist profile (Hernquist 1990). All N -body runs in this work used the same setup parameters as the GALAKOS disk, more details of which can be found in the original paper. For reference, the stellar disk has a mass of $4.8 \times 10^{10} M_{\odot}$ and a scale length of 2.67 kpc. The bulge has a mass of $8.1 \times 10^9 M_{\odot}$ and a scale length of 0.32 kpc. The dark matter halo has a mass of $10^{12} M_{\odot}$ and a scale length of 26.2 kpc.

The addition of the gas phase was done as follows. The version of `MakeNewDisk` used for the original GALAKOS model can generate a gas disk that is radially exponential and in vertical gravito-hydrodynamic balance. We modified the radial profile of this code in order to allow us to generate a disk with a constant surface density within some cutoff radius and then exponentially declining beyond that radius with the scale length of the stellar disk. Our fiducial model used an initial surface density of $20 M_{\odot} \text{pc}^{-2}$ and a cutoff radius of 9.3 kpc. This corresponds to an initial gas fraction of $\sim 16\%$. The initial gas disk is generated with a temperature of 10^4 K and solar metallicity.

After generating the gaseous disk in this way, we stitched the gas disk together with the GALAKOS N -body disk (and bulge and dark matter halo) after the GALAKOS disk had been allowed to evolve for 1.5 Gyr. The purpose of allowing the GALAKOS disk to evolve first for a short period of time was to allow for the bar to form unimpacted by the presence of the gas. We found that including the gas before the bar had formed disrupted the formation of the bar, as has been seen previously (e.g., Athanasoula et al. 2013). Throughout this work, we consider $t = 0$ for the N -body run to be the time at which we added the gas phase for the SMUGGLE run (i.e., we ignore the first 1.5 Gyr of evolution of the N -body disk when the bar is forming).

We made one additional modification when stitching the gas disk together with the N -body disk—we created a hole within the central 4 kpc of the gas disks. This hole guarded against an initial dramatic infall of gas within the bar region, which we found to destroy the bar. It is not uncommon for observed barred galaxies to have gas deficits in the bar region (though not in the very center; see Sellwood & Wilkinson 1993). Therefore, our practice of allowing the gas distribution to have a hole in the central region is consistent with our choice to begin the simulations with a bar already formed. In this manner, we are able to study the ensuing self-consistent interaction between the bar and the gas, but of course we are unable to explore the origin of bars in the presence of the gas.

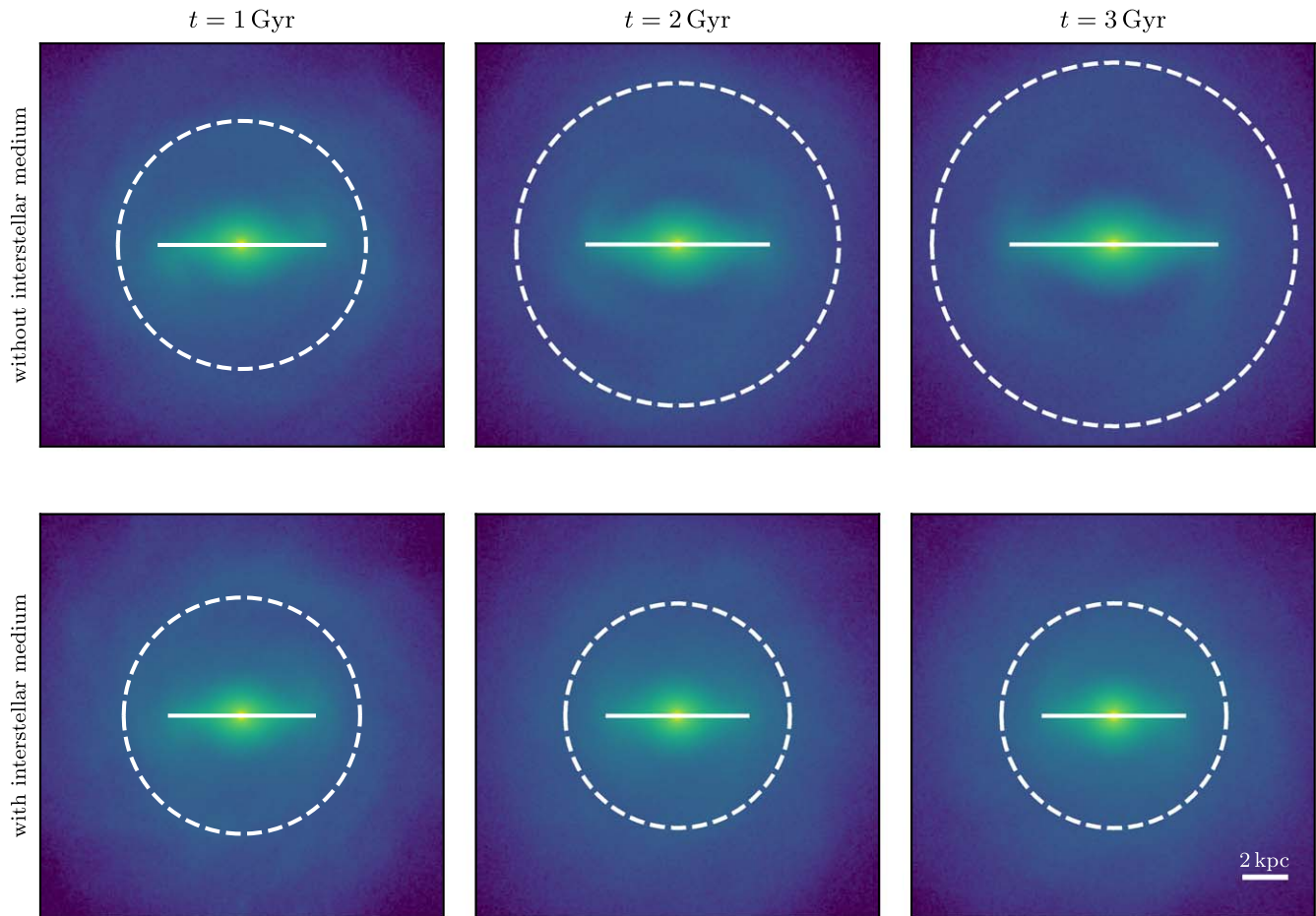


Figure 1. Stellar mass distribution of our simulations with and without the interstellar medium. The upper panels show an N -body-only simulation while the lower panels show a simulation that includes the SMUGGLE model for the interstellar medium. Each panel is 20 kpc to a side. The bar length is shown as a solid white bar (details on its computation are given in the text). The corotation radius is shown as a dashed white circle. Columns show different points in time, separated by 1 Gyr. We can see that, in the N -body run, the bar grows in length and strength. In the SMUGGLE run, the bar remains at approximately the same length and strength over the course of the simulation. The N -body model is identical to the GALAKOS model (with different particle numbers and softening lengths), as discussed in the text.

Our method for initializing gas was arrived at after numerous attempts to include enough gas in the simulation to be compatible with the Milky Way while also not destroying the bar. For example, we tried evolving an exponential gas disk adiabatically with the barred disk (i.e., no cooling, star formation, or feedback). Because there was no mechanism to remove gas from the central region, a large, highly pressurized pileup of gas formed in the center.⁹ We then turned on the full SMUGGLE model. As a result, there was a sudden collapse of gas to the center as pressure support was lost due to cooling and star formation. This abrupt change in the potential destroyed the bar.

We do not believe our method is the only nor even the best way to include gas. One advantage of our method, though, is that it approximates the expectation that in the bar region the gas surface density should be significantly reduced (e.g., Sellwood & Wilkinson 1993).

We used a mass resolution of $7.5 \times 10^3 M_{\odot}$ for the baryonic components (initial stellar disk, stellar bulge, and gas) and a

mass resolution of $3.75 \times 10^4 M_{\odot}$ for the dark matter halo. This mass resolution is closest to “level 3” in the AURIGA simulations (Grand et al. 2017). This corresponds to approximately 6.4×10^6 particles in the stellar disk, 1.1×10^6 in the bulge, 1.2×10^6 in the gas disk, and 25.3×10^6 in the dark matter halo. We used a softening length of 20 pc for all collisionless components. This softening length is smaller than that used in the original GALAKOS model (28 pc in their model, but ~ 43.5 pc when scaled to our mass resolution). Our smaller softening length is consistent with other resolved ISM models (Hopkins et al. 2018; Marinacci et al. 2019). However, as a consistency check, we reran our fiducial SMUGGLE run with 40 pc softening and found no difference in the pattern speed evolution of the bar. For the gas component, the softening length is fully adaptive with a softening factor of 2.5 (e.g., Weinberger et al. 2020). Snapshots were saved at equal intervals of 0.005 in the time units of the simulation, $\text{kpc}/(\text{km s}^{-1})$.

Our setup is initially out of equilibrium, but we found that, after about 500 Myr, the system has settled into a roughly steady-state configuration and initial transients appear not to affect the results after this point. The constant surface density of the initial gas disk is important for ensuring that the gas disk

⁹ We noticed that the bar slowed down in this adiabatic model, which lacks a mechanism to remove gas from the central region. Berentzen et al. (2007) also noted slowdown behavior in models that lacked central gas removal. It appears that gas removal from the center (in our model due to star formation) is necessary to stabilize a bar’s pattern speed.

is dense enough for comparisons to real galaxies to be appropriate.

2.2. Numerical Model

We use the SMUGGLE model (Marinacci et al. 2019) implemented within the moving-mesh, finite-volume hydrodynamics and gravity code AREPO (Springel 2010). The SMUGGLE model additionally includes radiative heating and cooling, star formation, and stellar feedback. Explicit gas cooling and heating of the multiphase interstellar medium is implemented, covering temperature ranges between 10 and 10^8 K.

Star formation occurs in cells above a density threshold ($n_{\text{th}} = 100 \text{ cm}^{-3}$) with a star formation efficiency of $\epsilon = 0.01$. Star formation converts gas cells into star particles that represent single stellar populations with a Chabrier initial mass function (Chabrier 2003). For each star particle, the deposition of energy, momentum, mass, and metals from stellar winds and supernovae is modeled. Photoionization and radiation pressure are handled using an approximate treatment. A more detailed description of this model can be found in the flagship SMUGGLE paper (Marinacci et al. 2019). A pedagogical review of cosmological simulations of galaxy formation can be found in Vogelsberger et al. (2020).

We used the fiducial model parameters, except that we increased the number of effective neighbors N_{ngb} for the deposition of feedback from 64 to 512. We found that a lower value of N_{ngb} resulted in inefficient photoionization feedback because the photoionizing budget had not been exhausted after deposition into 64 neighboring cells. We also employed an updated version of SMUGGLE using a new mechanical feedback routine similar to the one described in Hopkins et al. (2018). This updated routine is a tensor renormalization that ensures linear and angular momentum conservation to machine precision.

In addition to the SMUGGLE model, we considered a simpler model of the interstellar medium based upon Springel & Hernquist (2003). In this approach, the multiphase nature of the interstellar medium is described in a subgrid manner by allowing each resolution element to have a “cold” and a “hot” component, with the equation of state of the gas suitably modified. Gas is allowed to interchange between the cold and hot components through processes such as cooling and stellar feedback. Cold gas is allowed to undergo star formation. We refer to this model as the smooth interstellar medium model, and it is described in more detail in Marinacci et al. (2019).

2.3. Bar Analysis

The analysis of various bar properties is performed as follows. First, the pattern speed is measured from the angle of the second Fourier component. We measured the second Fourier component by computing

$$\begin{aligned} A_2 &= \sum_i m_i e^{i2\phi_i} \\ A_0 &= \sum_i m_i, \end{aligned} \quad (1)$$

where m_i and ϕ_i are the mass and azimuthal angle of each particle, respectively. We computed A_2 and A_0 in cylindrical bins of width 0.5 kpc from radii of 0 to 30 kpc. We defined the angle of the bar ϕ_b to be half the angle of the complex number

A_2 as measured in the bin extending from a radius of 2.5 to 3 kpc. After correcting for the periodicity of ϕ_b , we measured the pattern speed as one half of the two-sided finite gradient of ϕ_b as a function of time. We note that using the second Fourier mode is a blunt tool, discussed in Petersen et al. (2019a).

In order to compute other properties of the bar, it is necessary to decompose the disk into a barred and an unbarred component. We achieved this by following closely the methods described in Petersen et al. (2016, 2021). Our implementation is described in more detail in Appendix A. After the disk has been decomposed into a trapped and untrapped component, we measured the bar length as being the radius R_b , which encapsulates 99% of the stars identified as being trapped in the bar.

To compute torques, we used the tree algorithm in MakeNewDisk (Springel et al. 2005) customized to be accessible from Python using Cython. This algorithm is based on the TREESPH code (Hernquist & Katz 1989). We constructed a tree with an opening angle of 0.35 using only the star particles identified as being trapped in the bar. We then queried the tree at the locations of all resolution elements in the other components and computed the torque of the bar on such components. The torque on the bar by the other components is simply the negative of the torque on the other components by the bar. A similar analysis using basis function expansions was performed in Petersen et al. (2019b).

2.4. Plotting Details

We saved snapshots in intervals of 0.005 in the time units of the simulation, $\text{kpc}/(\text{km s}^{-1})$, which is very nearly equal to 1 Gyr (it is ~ 0.977 Gyr). Therefore, throughout this work, we refer to the native code time unit as Gyr. None of our results are sensitive to this choice. We applied a Savitzky–Golay filter (Savitzky & Golay 1964) as implemented in `scipy` using a window length of 21 and polynomial order of 3 to the plot of torques (Figures 2 and 9) and angle differences (Figure 5) in order to remove some numerical noise.

3. Results

We present the time evolution of different bar properties in Figure 2. In the upper panel, we show the pattern speed over time in the N -body (blue) and SMUGGLE (orange) runs. The pattern speed in the N -body case slows down while the pattern speed in the SMUGGLE case remains roughly constant. The slowing down of the pattern speed in the N -body case is consistent with a long line of numerical research on bars in N -body simulations (Hernquist & Weinberg 1992; Debattista & Sellwood 2000; Athanassoula 2002, 2003; Athanassoula & Misiriotis 2002; O’Neill & Dubinski 2003; Holley-Bockelmann et al. 2005; Martinez-Valpuesta et al. 2006; Weinberg & Katz 2007; Dubinski et al. 2009).

However, in the SMUGGLE case, the pattern speed remains constant. After the first Gyr of evolution, we find that the pattern speed increases by only $\sim 10\%$ over the next 4 Gyr, compared to a $\sim 43\%$ decrease in the pattern speed for the N -body run over the same interval.

The bottom panel of Figure 2 shows the torque exerted on the bar by different components. The solid lines indicate the torque on the bar by the dark matter halo, whereas the dashed line is the torque on the bar by the gas phase. In the N -body case, the halo exerts a steady negative torque on the bar, with

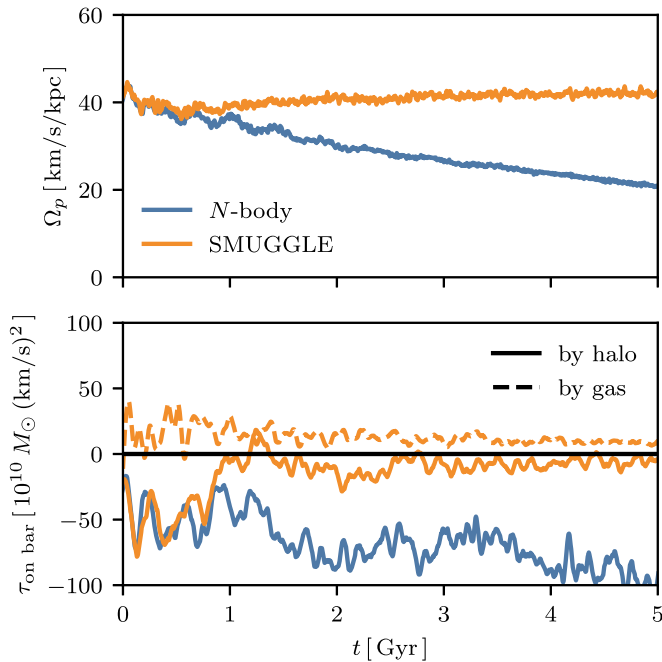


Figure 2. The upper panel shows the evolution of the pattern speed. As expected, the bar in the N -body run slows down due to interactions between the bar and the dark matter halo. However, the bar in the SMUGGLE run does not slow down and instead remains at a constant pattern speed. The lower panel shows the torque on the bar exerted by different components. The solid lines indicate the torque exerted by the halo in both the N -body and SMUGGLE cases. The dashed line is the torque exerted by the gas phase in the SMUGGLE run (there is no gas in the N -body run). After ~ 1 Gyr of evolution, the torque by the halo in the SMUGGLE case is severely reduced. We call this bar locking, and we discuss its proposed origin in Section 4. Details on the calculation of the torque and pattern speed are given in Section 2.3.

an average torque from 1 to 4 Gyr of -58.0 in units of $10^{10} M_{\odot} (\text{km s}^{-1})^2$. The halo in the SMUGGLE case exerts a similar negative torque on the bar in the first Gyr of evolution, but after that the halo exerts a much weaker torque on the bar, averaging only -7.8 in the same units and over the same time interval. The gas in the SMUGGLE case exerts a steady positive torque averaging 11.7 over 1 Gyr in the same units.

As we saw qualitatively in Figure 1, the upper panel of Figure 3 shows that the length of the bar in the N -body case grows over time while it remains roughly constant in the SMUGGLE case. This is also consistent with previous numerical work, which found that bars tend to grow as they slow down and the radius of corotation increases (Debatista & Sellwood 2000; Athanassoula 2003). The middle panel of Figure 3 shows the mass of the bar. As the N -body bar slows down and lengthens, it also grows in mass. The SMUGGLE bar, however, loses mass over time. This indicates a change in the bar’s angular momentum without a change in pattern speed, and highlights the fact that bars are not solid bodies and can respond to external torques through mass redistribution.

The time evolution of the bar strength, defined as the maximum of $|A_2/A_0|$ as a function of radius, is shown in the lower panel of Figure 3. The quantity $|A_2/A_0|$ varies from 0 to 1, with larger values indicating a stronger bar pattern. We see that, in the N -body case, $|A_2/A_0|$ increases over time as the bar pattern slows. This is consistent with previous N -body simulations that showed a clear correlation between the bar pattern speed and the bar strength (e.g., Athanassoula 2003). In the SMUGGLE case, we see that the bar strength has an initial

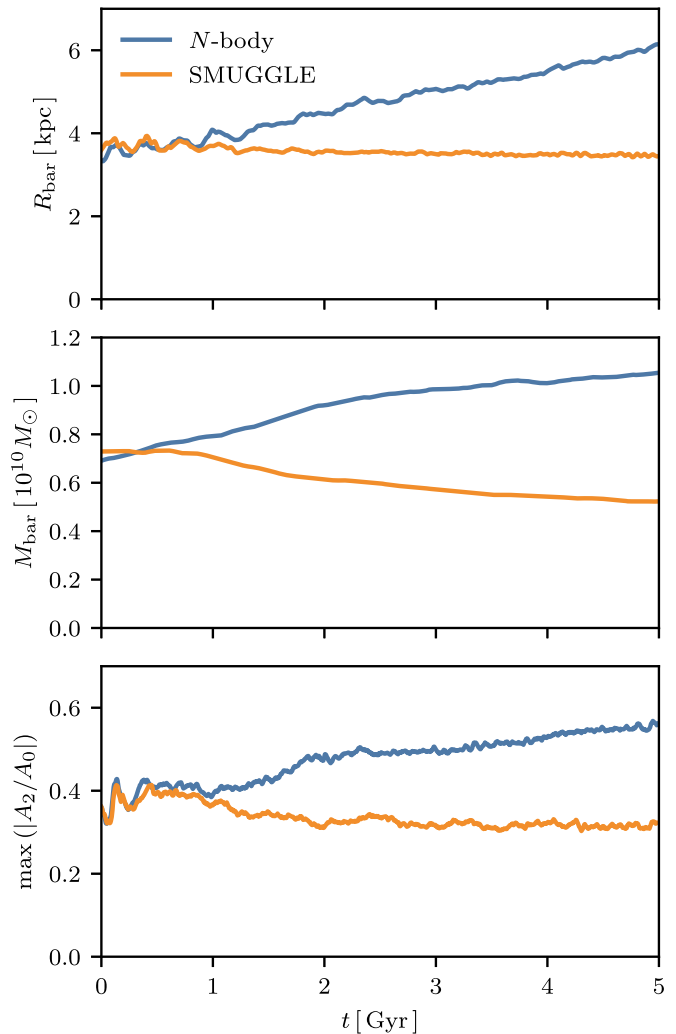


Figure 3. The evolution in bar length, mass, and strength. The upper panel shows the evolution of the bar length. In the N -body case, the bar lengthens. This occurs because, as the pattern speed drops, bar-like orbits at larger radii are possible. Stars are captured on these orbits, lengthening the bar. This process does not occur in the SMUGGLE cases because the bar pattern speed is not decreasing and therefore the bar length remains constant. The bar mass, shown in the middle panel, is increasing in the N -body case as the bar grows. It is decreasing in the SMUGGLE case, indicating mass redistribution without a change in pattern speed. The bar strength, shown in the lower panel, is measured as the maximum of the second Fourier component divided by the zeroth Fourier component. We see that, in the N -body case (blue), the bar strength increases with time, which is consistent with previous results showing that the bar strength increases as bars slow down. In the SMUGGLE case (orange), we see that the bar strength slightly decreasing with time. This is also consistent with the expected relation between pattern speed and strength, because the bar in this case is not slowing down.

drop but then remains at a roughly constant, but slightly decreasing, strength. This is consistent with the pattern speed in the SMUGGLE case being roughly constant or slightly increasing.

4. Discussion

4.1. Pattern Speed Evolution

The lack of evolution in the pattern speed of the SMUGGLE case (seen in Figure 2) is intimately tied to the sudden decrease in torque exerted on the bar by the dark matter halo.

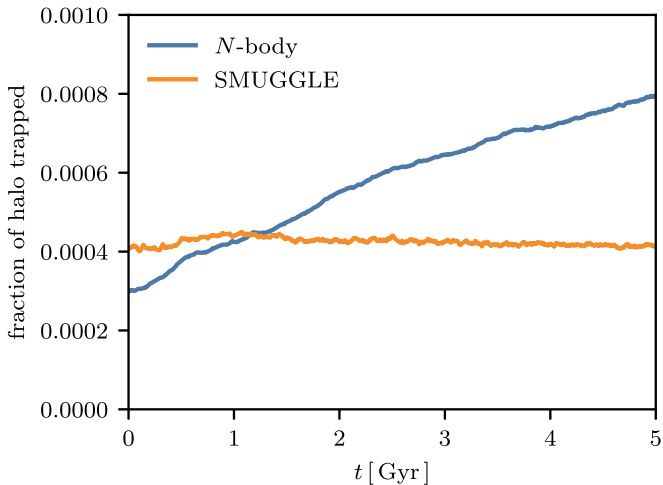


Figure 4. The halo mass fraction within two disk scale lengths (~ 5.3 kpc) trapped in the N -body and SMUGGLE runs. As the dark matter halo torques the bar, material from the halo is trapped on bar-like orbits. In the N -body case, the trapped fraction increases with time, indicating the torquing process is active and the bar is unlocked. In the SMUGGLE case, the trapped fraction is nearly constant with time, indicating the torquing process is inactive and the bar is locked.

We interpret this behavior in terms of the halo wake mechanism. In the N -body case, a well-known phenomenon is that the halo material resonant with the bar forms a wake, and this wake lags behind (Tremaine & Weinberg 1984b; Weinberg 1985; Hernquist & Weinberg 1992) and exerts a negative torque on the bar, slowing it down (see Figure 5 below).¹⁰ As the bar slows down, the location of the resonances in the phase space changes (see Figure 12 and Table 1 in D’Onghia & Aguerri 2020) allowing halo material newly resonant with the bar to participate in the formation of the wake. However, the gas is also a reliable source of positive torque on the bar, speeding the bar up. In turn, this stops the location of the resonance from changing such that the halo cannot reinforce the wake, therefore arresting the process by which the halo can slow the bar down. We term this process “bar pattern speed locking,” or simply bar locking for short.¹¹

This bar-locking process is similar to the “metastability” effect, which has been previously discussed in the literature (Valenzuela & Klypin 2003; Sellwood & Debattista 2006). Finally, we also note that these authors, in particular, observe that the effects of numerical resolution in the simulations adopted to explore these mechanisms have yet to be fully explored and could play a role in the observed phenomenology of the simulations. We plan to address these issues in future dedicated work.

We test this interpretation in two ways. First, we measure the fraction of mass trapped in the halo. As material in the halo wake torques the bar, that material becomes trapped on bar-like orbits (the “shadow bar”; Petersen et al. 2016). In Figure 4, we show the halo trapped fraction for particles with radii less than two disk scale lengths (~ 5.3 kpc). In the N -body case, the

¹⁰ Since the bar is not a solid body, it is not guaranteed that a negative torque will slow it down—e.g., a negative torque could reduce the mass of the bar, reducing its moment of inertia without changing its pattern speed. However, the bar empirically seems to slow down in response to a negative torque induced by a halo wake.

¹¹ To be more explicit, it is the gas which locks the pattern speed of the bar. The gas does this by forcing the resonant locations of the bar into regions of the halo phase space that can no longer support significant negative torque.

trapped fraction increases with time, as expected because the halo is actively torquing the bar (which is, therefore, unlocked). In the SMUGGLE case, the trapped fraction is constant (or perhaps slightly decreasing) with time (indicating the bar is locked). This supports our interpretation that the halo wake process has shut down in the presence of the gas phase.

Second, we measure the angle offset between the halo wake and the bar. If the wake and the bar are aligned (i.e., there is no angle offset), then the wake cannot exert a negative torque on the bar. This angle is plotted in the left panel of Figure 5, which shows that the angle offset is larger in the N -body case than in the SMUGGLE case by about a factor of three. The center and right panels of Figure 5 show the halo wake with respect to the location of the bar in the N -body (center) and SMUGGLE (right) cases at one point in time. We note that, in Figure 5, we have removed the halo material trapped in the bar, which exerts no net torque on the bar.

The presence of the gas can arrest the process by which additional material in the dark matter halo can contribute to a wake. However, this does not explain why the pattern speed in the SMUGGLE case is nearly constant over several Gyr. Naively, it would seem to be a coincidence that the bar pattern speed remains constant in the SMUGGLE case, resulting from a chance cancellation of the halo and gas torques. However, a constant pattern speed in the presence of gas has been observed in a few simulations of barred galaxies with gas (Friedli & Benz 1993; Berentzen et al. 2007; Villa-Vargas et al. 2009, 2010; Athanassoula 2014).

Friedli & Benz (1993) argue this behavior is due to the steepening of the circular velocity curve in the central region as the bar drives gas to the center. Villa-Vargas et al. (2009) argue this behavior occurs when the corotation resonance is larger than the disk radius, but we observe the behavior when the corotation radius is well within the disk.

We propose that an equilibrium mechanism is responsible for the pattern speed remaining approximately constant. In this scenario, residual negative torque from the dark matter halo balances out the positive torque from the gas phase. It has been shown that, when an analytic bar is forced to rotate at a constant pattern speed for a few Gyr, the halo exerts almost no torque on the bar (Chiba & Schönrich 2022). We saw in Figure 2 that the dark matter halo in our simulation is still able to support some negative torque over a several Gyr time span.

We argue that the following occurs. First, the bar is not able to slow down quickly enough, due to the positive torque of the infalling gas. This causes the resonant halo phase space at a particular pattern speed, $\Omega_{p,0}$, to become mixed and no longer able to support a negative torque.¹² Second, the gas is still exerting a positive torque on the bar, and therefore the pattern speed will again increase. At higher pattern speeds, the halo has not yet been totally mixed, and therefore the halo will once again be able to exert a negative torque on the bar. The pattern speed will then settle at a new value slightly higher than $\Omega_{p,0}$, where the gas and halo torques cancel. Over time, the pattern speed should slowly increase.

4.2. Delayed Gas Injection

A clear prediction of our proposed mechanism is that the constant pattern speed at which particular galaxy will end up is

¹² In the halo wake picture, this corresponds to the wake becoming fully aligned with the bar.

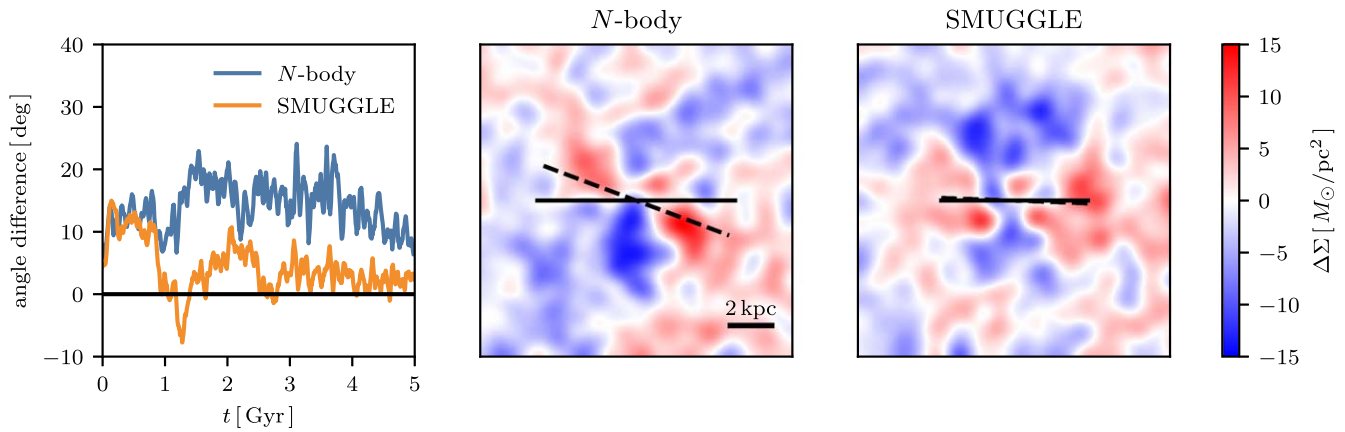


Figure 5. The wake excited in the dark matter halo. The dark matter halo wake is shown in the *N*-body case (middle panel) and SMUGGLE case (right panel) after 2.6 Gyr of evolution. The middle and right panels show a surface density projection in the *x*-*y* plane of the dark matter halo after an axisymmetric average has been subtracted. The solid line indicates the direction of the bar, while the dashed line indicates the direction of the halo wake (both measured by taking the second Fourier component within a sphere of all material within a radius of 4 kpc). The left panel shows the time evolution of the angle difference between the bar and the halo wake, as measured from the second Fourier component. After the first Gyr, the angle difference in the SMUGGLE case is smaller than in the *N*-body case by about a factor of two, reflecting how the dark matter halo in the SMUGGLE case is unable to exert as negative a torque on the bar as in the *N*-body case.

somewhat arbitrary. In the real universe, for an isolated galaxy, it would be the formation pattern speed of the bar, while in our simulation, it is the pattern speed of the bar when gas is added to the system. We tested this by adding gas to the system at a later time when the bar has further grown and slowed down with time. In our particular test, we added the gas at a time when the pattern speed is $\sim 30 \text{ km s}^{-1} \text{ kpc}^{-1}$. As shown in Figure 6, we find that the pattern speed evolution is very similar between the two cases (orange and red lines). If anything, the system with a lower pattern speed seems to speed up more, which is consistent with our picture because the stronger bar should experience a larger torque from the gas, as it is more efficient at driving gas inflows. We also show in the Appendix B that more slowly rotating bars at fixed bar strength are more efficient at driving gas inflows as well. Nonetheless, when the initial pattern speed is lower (red line), the addition of gas does not cause the pattern speed to quickly return to the higher value of our fiducial simulation (orange line).

4.3. Varying Initial Gas Fractions

We performed a test in which we varied the initial gas fraction of the disk. In our fiducial run, we set the surface density of the gas disk from 4 to $\sim 9.3 \text{ kpc}$ to be $20 M_{\odot} \text{ pc}^{-2}$. We also ran with surface densities of 15, 10, and $5 M_{\odot} \text{ pc}^{-2}$. These correspond to initial gas fractions of approximately 16%, 10%, 7%, and 4%. The pattern speed evolution is shown in Figure 7. We find that the bar in disks with initial surface densities of 20, 15, and $10 M_{\odot} \text{ pc}^{-2}$ evolve with a constant pattern speed, while the bar in a disk with initial surface density of $5 M_{\odot} \text{ pc}^{-2}$ slows down at a rate similar to that in the *N*-body case.

After 5 Gyr, the $10 M_{\odot} \text{ pc}^{-2}$ simulation has a gas fraction of 5.7% but still exhibits constant pattern speed behavior. As a result, we conclude that for the disk, bar, and halo properties considered in this work, a gas fraction of only approximately 5% is necessary in order for the proposed stabilizing mechanism to operate. We stress that this gas fraction threshold is only for the system considered in this work. Systems with different structural parameters may require a different

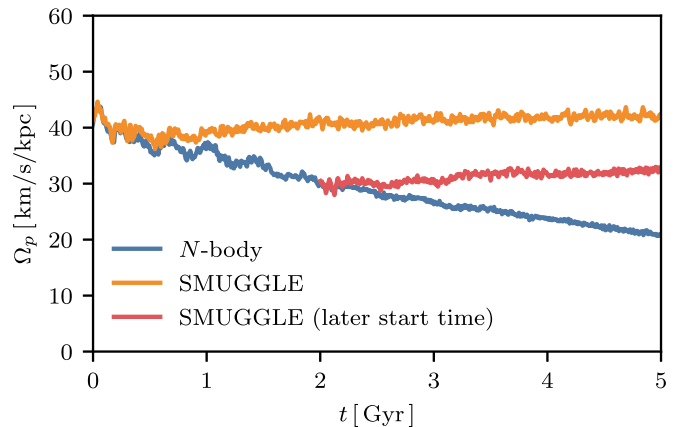


Figure 6. Pattern speed evolution with a lower initial pattern speed. We tested the evolution of our system when gas is added to the *N*-body run at a later time, but with all other simulation parameters kept the same. The setup is therefore identical to our previous runs, just with a bar that is larger and stronger, and with a lower pattern speed. We find that the pattern speed evolution is very similar to our fiducial case, except that the bar retains its original pattern speed. This indicates a mechanism that keeps the bar at its formation pattern speed, and that there is not a particular pattern speed that the system tends to.

threshold. For example, Aumer & Schönrich (2015) find slowdown behavior in a barred disk initially 10 times less massive than ours with a gas fraction of 10%. To make things more complicated, Villa-Vargas et al. (2010) find that the gas fraction cutoff varies with the softening length used. Determining exactly how the gas fraction cutoff varies with these properties deserves further attention.

4.4. Semi-analytic Model

We also developed a simple semi-analytic model of a bar-disk-halo system. This exercise demonstrates that our proposed mechanism follows from a few simple assumptions. Our method follows closely the one developed in Chiba & Schönrich (2022). We model the bar-disk-halo system with three components: a dark matter Hernquist (1990) halo, a Miyamoto & Nagai (1975) disk, and a pure quadrupole bar

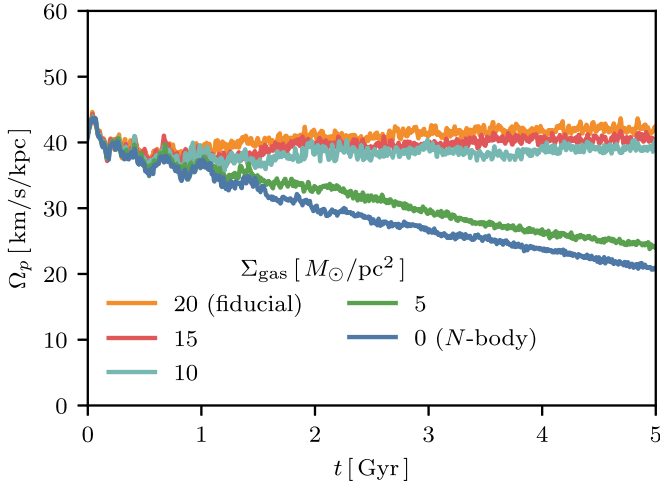


Figure 7. Pattern speed evolution with varying gas fractions. We explored the impact of lowering the initial gas surface density of our fiducial disk on the evolution of the pattern speed. The surface densities we tested, i.e., 20, 15, 10, and $5 M_{\odot} \text{pc}^{-2}$, correspond to initial gas fractions of 16%, 10%, 7%, and 4%. We find that initial surface densities 20, 15, and $10 M_{\odot} \text{pc}^{-2}$ result in bars that remain at a constant pattern speed, while an initial surface density of $5 M_{\odot} \text{pc}^{-2}$ results in a bar that slows down in roughly the same manner as the N -body case.

described in Chiba & Schönrich (2022). The bar and disk components are just described by their potential, but we integrate the trajectories of test particles drawn from a Hernquist halo. It should be noted that we do not include the interactions between these test particles, and so this model is not self-consistent. We give our chosen parameter values in Appendix E.

We allow the bar in this model to rotate as a solid body. However, we crucially allow the pattern speed of the bar to freely change with time in accordance with the torque exerted on the dark matter halo by the bar. In particular, we subtract the z -component of this torque divided by the moment of inertia of the bar from the pattern speed at each time step. Because the radius of corotation R_{CR} is a parameter in the bar model from Chiba & Schönrich (2022), we allow the moment of inertia of the bar to vary with R_{CR}^2 . This is inspired by the fact that the moment of inertia of an ellipsoid scales with the sum of the square of its axes. To be more precise, we allow

$$I = \frac{I_6}{10^{10} M_{\odot} (\text{km s}^{-1})^2} \left(\frac{R_{\text{CR}}}{6 \text{ kpc}} \right)^2, \quad (2)$$

where I_6 is a free parameter chosen by the user. We found that allowing $I_6 = 8$ is a good approximation to our fiducial disk model. In code units, the moment of inertia of the SMUGGLE bar (i.e., the particles classified as being in the bar) is about 2. This is a factor of 4 smaller than our fiducial value of $I_6 = 8$, but this is probably due either to the fact that the bar does not really rotate as a solid body or that resonantly captured stars contribute to the real bar’s effective moment of inertia (Weinberg 1985).

In addition to I_6 , we allowed for another free parameter—the torque from the gas phase on the bar, τ_{gas} . This torque is applied to the bar in the same way as the torque from the halo is applied. The torque is given in code units ($10^{10} M_{\odot} (\text{km s}^{-1})^2$).

We show the effect of varying the gas torque τ_{gas} from 0 to 20 in increments of 2 in Figure 8. The solid lines indicate the

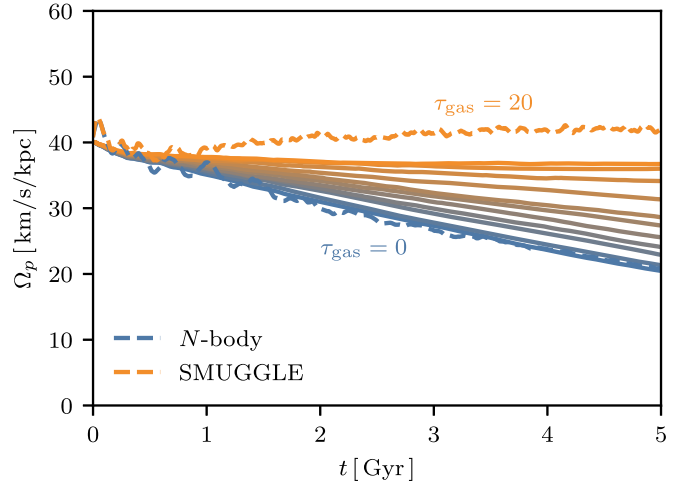


Figure 8. A comparison between the pattern speeds of our fiducial disk systems and a semi-analytic model. The solid lines indicate the pattern speeds, assuming a constant positive torque, varying in increments of 2 from 0 to 20. The dashed lines indicate the pattern speed evolution from our fully self-consistent simulations from earlier. We find excellent agreement between our fiducial simulations and our semi-analytic model of a bar–disk–halo system. Torques are given in code units ($10^{10} M_{\odot} (\text{km s}^{-1})^2$).

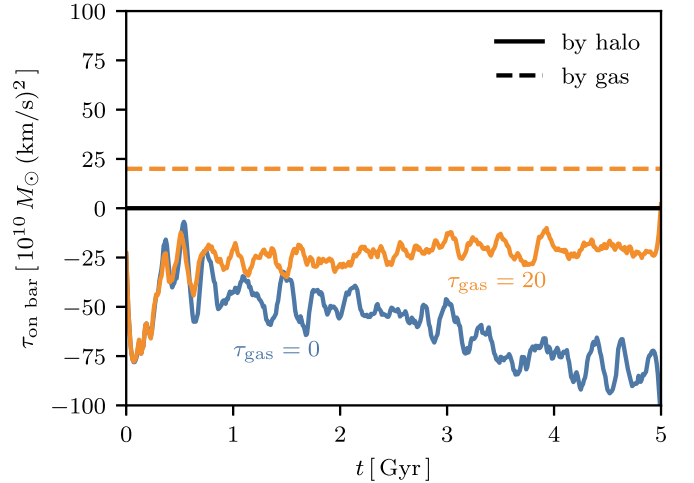


Figure 9. The torque exerted on the bar by various components in our semi-analytic model. Solid lines indicate the torque by the halo, while the dashed line indicates the torque exerted by the gas phase. We chose two models with $\tau_{\text{gas}} = 0$ and 20, which most closely resemble our N -body and SMUGGLE disks, respectively. This figure ought to be compared to the lower panel of Figure 2. Overall, we find good qualitative agreement.

semi-analytic model, while the two dashed lines correspond to our fiducial simulations introduced earlier. For reference, the average torque exerted by the gas phase on the bar in our fiducial simulation was 11.7 in code units. We see in Figure 8 that we can reproduce the stability of our fiducial gas disk (i.e., its lack of secular evolution) simply by including a positive torque on the order of 6. Our semi-analytic model with no gas torque can reproduce the pattern speed evolution of the N -body case.

We next take the $\tau_{\text{gas}} = 0$ and 20 cases from Figure 8 and plot the halo torque evolution. This result, given in Figure 9, is comparable to the lower panel of Figure 2. We find that the $\tau_{\text{gas}} = 0$ case compares favorably to the N -body case described in previous sections. The bar exerts a steady negative torque in this case (blue line). When a gas torque is included (orange

lines), we find that the halo’s torque becomes much weaker, similar to what we found in the SMUGGLE case. The gas applies a steady positive torque by construction. Therefore, the locking process is reproduced in our simple semi-analytic model. Curiously, we do not see the bimodal behavior in Figure 7 and described in Villa-Vargas et al. (2010). It is not presently clear why this is the case.

4.5. Observations

Observational estimates of the pattern speeds of bars indicate that nearly all galaxies have $1 < \mathcal{R} < 1.4$ (Corsini 2011; Aguerri et al. 2015; Guo et al. 2019; Garma-Oehmichen et al. 2020), where \mathcal{R} was defined in Section 1 to be $\mathcal{R} \equiv R_{\text{CR}}/R_b$. This observational fact has long been in conflict with the theoretical expectation that bars should slow down, increasing \mathcal{R} (e.g., Tremaine & Weinberg 1984b; Weinberg 1985; Debattista & Sellwood 2000). Explanations for this discrepancy have been given in the past. Some have argued that perhaps the central regions of dark matter halos are less dense than we expected from Λ CDM (e.g., Debattista & Sellwood 2000; Fragkoudi et al. 2021). Some have argued that perhaps bars are recurrent, short-lived phenomena, and that all the bars we see in the local Universe are very young (Bournaud & Combes 2002; Bournaud et al. 2005). Some have argued that modifications to General Relativity ease the tension between the observed universe and Λ CDM (e.g., Roshan et al. 2021a, 2021b).

Because such a small gas fraction is necessary for our stabilizing mechanism to operate (5% in our Milky Way–like disk), we argue that most galaxies host a bar that is not slowing down. This naturally explains why most observed bars are fast rotators. However, we acknowledge two instances of reported discrepancies between our mechanism and observations.

First, we note that Garma-Oehmichen et al. (2020) found that the rotation parameter \mathcal{R} positively correlates with gas fraction, such that galaxies with higher gas fractions are rotating more slowly. However, it is not obvious this is in tension with our result, because the gas fraction of galaxies correlates with other galactic properties (Blanton & Moustakas 2009). Furthermore, the measurement of pattern speeds is a delicate process still prone to large errors.

Second, the works of Chiba et al. (2021) and Chiba & Schönrich (2021) have made indirect measurements of the deceleration of the bar’s pattern speed from kinematics and chemistry. We point out that these reported measurements are not direct measurements of the Milky Way bar’s deceleration. For instance, Chiba et al. (2021) measure the pattern speed based on the asymmetry of the Hercules stream, but this can also be produced by spiral arms (Hunt et al. 2018). Much like the simulations in the present work, the simulations of these two works do not properly account for the complicated formation process of the Galactic bar, which may leave imprints on the present-day distribution of stars in spatial, kinematic, and chemical space. More investigation is necessary to reconcile the present work with these two well-executed manuscripts.

Lenticular galaxies that lack a significant gas phase offer an opportunity to find slowly rotating bars. It would still take several Gyr for a galaxy hosting a fast bar to transition to the slow bar regime, so slow bars should only occupy lenticular galaxies that have been lenticular for some time. NGC 4277 is one such example, whose bar has been found to rotate with

$\mathcal{R} \sim 1.8$ (Buttitta et al. 2022). On the other hand, NGC 4264 has a fast bar with $\mathcal{R} \sim 1$ (Cuomo et al. 2019). The difference has been explained by differences in the dark matter content of the galaxies (Buttitta et al. 2023). We offer another explanation based on the timing of when gas was stripped from these galaxies.

There are further examples of gas-rich galaxies hosting slow bars. For example, UGC 628 ($\mathcal{R} \sim 2$; Chemin & Hernandez 2009) and NGC 2915 ($\mathcal{R} > 1.7$; Bureau et al. 1999). UGC 628 has been studied in detail by Chequers et al. (2016), who note that it indeed has a low gas fraction for galaxies of its type. NGC 2915 has a gas fraction of 70% (Werk et al. 2010), which would seem to be in conflict with our prediction that only a 5% gas fraction is necessary to arrest the halo slowdown process. However, NGC 2915 has significantly different structural properties than the Milky Way–like model we considered in this work. In particular, it has a significantly lower mass ($\sim 10^9 M_\odot$ compared to $4.8 \times 10^{10} M_\odot$ in our model). Further work is necessary to see how the gas fraction threshold varies with galactic properties.

Fraser-McKelvie et al. (2020) find that quenched galaxies tend to host longer bars than star-forming galaxies. This provides some support for our proposed mechanism, because there is evidence quenching can occur through gas depletion (e.g., Whitaker et al. 2021). However, this correlation could be explained simply by the fact that longer bars ought to be more efficient at quenching their host galaxies (e.g., Gavazzi et al. 2015).

Finally, we mention the evolution of \mathcal{R} in our simulation. In the N -body simulation, the bar forms with $\mathcal{R} \sim 1.6$ at $t = 0$ Gyr, which is already well within the slow bar regime. After 5 Gyr of evolution, \mathcal{R} has risen to ~ 1.9 . In the SMUGGLE simulation, the gas is added to the $t = 0$ Gyr snapshot, so it begins with $\mathcal{R} \sim 1.6$. As expected, after 5 Gyr of evolution, \mathcal{R} is still ~ 1.6 . However, this relies on our measure of the bar length as being the maximum radius of all orbits trapped in the bar, which is not an observationally accessible measure of bar length. One would need to test different observationally possible bar length estimators, such as ellipse fitting (Athanasoula et al. 1990; Márquez et al. 1999; Athanasoula & Misiriotis 2002; Michel-Dansac & Wozniak 2006; Aguerri et al. 2009, 2015). This is beyond the scope of our current work. Nonetheless, our prediction that \mathcal{R} is stable in the presence of sufficient gas is robust. Assuming bars form with $\mathcal{R} \sim 1$, we predict this should remain the case with further evolution. Why the N -body simulation forms a bar with $\mathcal{R} \sim 1.6$ is a separate question deserving further attention.

4.6. Previous Idealized Simulation Work

Substantial work has been devoted to the role of gas in bar dynamics. We discuss this and highlight the novel aspects of the present investigation.

To our knowledge, the first work on a barred galaxy with a gas component was by Friedli & Benz (1993). They found a stable pattern speed when a dissipative component was added to the system, with a slight increase in the pattern speed near the end of their simulation. However, their model was only evolved for ~ 1 Gyr, so it is unclear if their bar exhibits a stable pattern speed over several Gyr.

Berentzen et al. (2007) describe a model containing up to 8% gas. Their disk is similar to ours (though their dark matter halo is a factor of 10 less massive). They find slowdown behavior up

to a gas fraction of 8%, with the finding that higher gas fractions lead to a reduced slowdown. However, for the models for which they show pattern speeds, they do not include star formation nor the removal of gas from the center of their disk. In preliminary work, we found slowdown behavior in an adiabatic model with similar gas fractions but lacking any method for removing gas from the central region (in our fiducial SMUGGLE model, this is achieved through star formation). We surmise that the removal of gas from the central region is an important requisite for stable pattern speeds, though a careful torque analysis is necessary to confirm this hypothesis.

Villa-Vargas et al. (2010) do find stable pattern speeds in models with gas fractions as low as 8% (depending on the force softening used). Crucially, their model does contain a routine for removing gas from the central region of the disk. These authors state the behavior is bimodal, with a clear stable regime and a slowdown regime. These authors make no mention of the process by which the halo braking process is arrested, as we propose in the present paper.

Athanassoula et al. (2013) and Athanassoula (2014) find stable evolution in \mathcal{R} for a triaxial halo over 10 Gyr with initial (final) gas fractions of 100% (7%), 75% (6%), and 50% (5%). For a model with 20% (3%) gas fraction, they find an increasing \mathcal{R} . In their model with a spherical halo, they always find increasing \mathcal{R} , contrary to the present work. We note there is a structural difference in their dark matter halo. They use a cored isothermal sphere as opposed to our Hernquist halo. It is not clear to us what impact this would have on the expected torque from the halo (i.e., the velocity structure of their halo may allow for more efficient capture and thus stronger torquing). The bar-locking process (or a similar mechanism) that we propose in this paper is not mentioned by these authors.

There may also be issues related to structural differences between their bars and the bar considered in this work. In our case, we allowed the bar to form in an N -body run and then added gas after the bar formation. In Athanassoula et al. (2013) and Athanassoula (2014) the bar forms from a disk that is initially gas-rich. Neither approach is inherently better, but it is known that, in the latter case, the resultant bar strength is weaker for initially gas-rich systems (e.g., Athanassoula et al. 2013). Weaker bars are less efficient at driving gas inward (Regan & Teuben 2004) and thus should experience less positive torque from the gas phase. A direct comparison based on the torque by the gas phase on the bar is necessary.

Aumer & Schönrich (2015) describe a model containing gas and stars that slows down with time. In their model, gas is added to the system to target a gas fraction of 10%. Their disk is initially a factor of 10 less massive than the disk considered in this work, but they grow their disk to be about the same mass as ours. They find their bar lengthens and slow down with time, which they attribute to the dark matter halo slowdown dominating over the gas inflow. However, it may also be the case that a bar in a disk grown in their way naturally extends its length as fresh material to be captured by the bar is added to the system. A useful experiment would be to grow a barred disk with a static dark matter halo to see if its pattern speed evolution mimics theirs, to determine if their lengthening and slowing down is truly attributable to the halo friction.

However, their disk is about a factor of 10 less massive than the disk considered in this work. The necessary gas fraction for a stable pattern speed probably depends on galaxy properties

like mass. It is unclear whether 10% is sufficient for their bar to have a stable pattern speed.

4.7. Cosmological Simulations

Barred galaxies in cosmological simulations of galaxy formation continue to be in conflict with observations by producing bars that rotate too slowly (Algorry et al. 2017; Peschken & Łokas 2019; Fragkoudi et al. 2021; Frankel et al. 2022).¹³ These works examine bars in EAGLE (Crain et al. 2015; Schaye et al. 2015), Illustris (Vogelsberger et al. 2014a, 2014b), and Illustris TNG50 (Nelson et al. 2019; Pillepich et al. 2019). Okamoto et al. (2015) describe cosmological zoom simulations of two barred Milky Way–like galaxies that both slow down over time. As pointed out by Villa-Vargas et al. (2010), the gas fraction cutoff for the stable pattern speed regime increases with lower softening lengths. Okamoto et al. (2015) use softening lengths larger than ours by about a factor of 6. This highlights the importance of future work exploring precisely when barred galaxies ought to be in the stable regime.

Fragkoudi et al. (2021) explored the evolution of bars in the Auriga cosmological zoom simulations (Grand et al. 2017). They find \mathcal{R} values consistent with observations. Furthermore, their pattern speed evolution shows some apparent periods of stability (see their Figure B1). One galaxy, Au26, appears to even transition from the stable pattern speed regime to the slowing-down regime at a lookback time of ~ 1.8 Gyr.

Furthermore, the pattern speeds of bars in both cosmological simulations and the real universe can be affected by environmental processes not included in our simulation—e.g., satellite infall (Purcell et al. 2011), non-sphericity (Athanassoula et al. 2013), rotation in the dark matter halo (Saha & Naab 2013; Long et al. 2014; Collier et al. 2018, 2019), or perhaps even the gaseous circumgalactic medium. Naturally, extending our present work to account for such effects is a crucial next step in understanding the formation and evolution of galactic bars. We are presently engaged in such an exploration.

5. Conclusions

We performed a simulation of a Milky Way–like galactic disk hosting a strong bar with a state-of-the-art model for the interstellar medium. We found that the pattern speed of the bar in this simulation does not slow down but rather remains at a stable, constant pattern speed. We provided a simple semi-analytic model that reproduces many of the features from our fiducial disk model.

The implications of our findings are numerous. First, we naturally explain why nearly all observed galaxies are fast rotators without requiring the inner regions of dark matter halos to be underdense (Debattista & Sellwood 1998, 2000) or requiring new physics (Roshan et al. 2021a, 2021b). Second, we show that the role of gas is of paramount importance in studies that attempt to uncover the nature of dark matter from its effect of slowing down the bar (Chiba & Schönrich 2021; Chiba et al. 2021). Third, we provide an explanation for how the Milky Way’s bar could be both long-lived and a fast rotator, for which there is some observational evidence (Bovy et al. 2019). Finally, we complicate the picture of stellar radial

¹³ Though see Frankel et al. (2022), who argue bars have consistent pattern speeds with observations, but are too short.

mixing expected to sculpt the Milky Way’s disk (Bird et al. 2012; Hayden et al. 2015), a process that relies upon the pattern speed of the bar to change with time. The radial mixing of the gas phase induced by the bar, as predicted in Hopkins & Quataert (2011), might have implications for the radial metallicity gradients of galaxies. Our work does not alter expectations for radial mixing induced by spiral arms (Sellwood & Binney 2002).

We found that, below a certain gas fraction, bars should still be able to slow down. Therefore, we expect barred spiral galaxies that have been gas-poor for extended periods of time to be rotating very slowly. We therefore predict that observations that target such galaxies (e.g., lenticular barred galaxies; Blanton & Moustakas 2009) would find slowly rotating bars.¹⁴ There do exist examples of galaxies known to be slow rotators—the low surface brightness galaxy UGC 628 (Chemin & Hernandez 2009), lenticular galaxy NGC 4277 (Buttitta et al. 2022), and NGC 2915 (Bureau et al. 1999). UGC 628 has been studied in detail by Chequers et al. (2016), who note that it indeed has a low gas fraction for galaxies of its type. NGC 2915 has a gas fraction of 70% (Werk et al. 2010), which would seem to be in conflict with our prediction that only a 5% gas fraction is necessary to arrest the halo slowdown process. However, NGC 2915 has significantly different structural properties than the Milky Way–like model we considered in this work, as discussed in Section 4.5. We predict a general trend that bars in gas-rich spiral galaxies should rotate quickly, while some bars in gas-poor spiral galaxies should rotate slowly.

Snapshots at 500 Myr cadence are publicly available on Zenodo: doi: [10.5281/zenodo.8061363](https://doi.org/10.5281/zenodo.8061363).

Acknowledgments

We would like to thank the referee, Michael S. Petersen, for a thorough report that greatly strengthened the arguments in our work. We would like to thank Greg L. Bryan, Neal J. Evans, Drummond B. Fielding, Keith Hawkins, Jason A. S. Hunt, Sarah M. R. Jeffreson, Kathryn V. Johnston, Peter M. W. Kalberla, Jürgen Kerp, Julio F. Navarro, Dylan Nelson, Suchira Sarkar, Joshua S. Speagle, Martin D. Weinberg, and Yanfei Zou for helpful discussions. A.B. would like to thank Todd Phillips for helpful discussions. Some computations in this paper were run on the FASRC Cannon cluster supported by the FAS Division of Science Research Computing Group at Harvard University. Resources supporting this work were also provided by the NASA High-End Computing (HEC) Program through the NASA Advanced Supercomputing (NAS) Division at Ames Research Center. This research has made use of the Spanish Virtual Observatory (<https://svo.cab.inta-csic.es>) project funded by MCIN/AEI/10.13039/501100011033/ through grant PID2020-112949GB-I00. A.B. was supported by the Future Investigators in NASA Earth and Space Science and Technology (FINESST) award number 80NSSC20K1536 during the completion of this work. E.D. was partially supported by HST grants HST-AR-16363.001 and HST-AR-16602.006-A and by NASA Award NASA 80NSSC22K0761. J.Q. acknowledges support from NSF grant AST-2008490. L.V.S. is grateful for financial support from NASA ATP

¹⁴ This does not mean that we predict *all* gas-poor galaxies should be slowly rotating. Indeed, they would need to be gas-deficient for several Gyr before they would be classified as slow rotators.

80NSSC20K0566, NSF AST 1817233, and NSF CAREER 1945310 grants. P.T. acknowledges support from NSF grant AST-1909933, AST-2008490, and NASA ATP Grant 80NSSC20K0502. M.V. acknowledges support through NASA ATP 19-ATP19-0019, 19-ATP19-0020, 19-ATP19-0167, and NSF grants AST-1814053, AST-1814259, AST-1909831, AST-2007355, and AST-2107724.

Software: AGAMA <https://github.com/GalacticDynamics-Oxford/Agama>, ASTROPY (Astropy Collaboration et al. 2013, 2018), H5PY <http://www.h5py.org/>, INSPECTOR_GADGET https://bitbucket.org/abauer/inspector_gadget/, JOBLIB <https://joblib.readthedocs.io/en/latest/>, MATPLOTLIB (Hunter 2007), NUMBA (Lam et al. 2015), NUMPY (Harris et al. 2020), SCIPY (Virtanen et al. 2020), TQDM <https://tqdm.github.io/>.

Appendix A Bar Decomposition

Computing the length of the bar and the torque on the bar by different components requires us to decompose the disk into a component that is trapped by the bar and a component that is untrapped. In order to do this, we follow closely the technique developed in Petersen et al. (2016). We analyzed the orbit of each star particle (meaning initial disk, bulge, and newly formed stars) by extracting the x - y positions of the apoapse of each in a frame corotating with the bar, where apoapses are defined as local maxima in r . For each apoapse, we searched for the 19 closest apoapses in time and applied a k -means clustering algorithm on this set of 20 points with $k = 2$. We then computed for each of the two clusters the average angle from the bar $\langle \Delta\phi \rangle_{0,1}$, the standard deviation in R of the points $\sigma_{R0,1}$, and the average radius of the cluster $\langle R \rangle_{0,1}$. At each apoapse, a particle was considered to be in the bar if it met the following criteria:

$$\max(\langle \Delta\phi \rangle_{0,1}) < \pi/8 \quad (\text{A1})$$

$$\frac{\sigma_{R0} + \sigma_{R1}}{\langle R \rangle_0 + \langle R \rangle_1} < 0.22. \quad (\text{A2})$$

These criteria are slightly different and simplified from the ones used in Petersen et al. (2016), but empirically we found them to work well at decomposing the disk into a bar and disk component. In Figure 10, we show an example of this decomposition. The *left* panel shows a surface density projection of the stellar disk and bulge (including newly formed stars) from the SMUGGLE model after 1 Gyr of evolution in a frame such that the bar is aligned with the x -axis. The *middle* panel shows a projection of the subset of stars that are identified as being trapped in the bar, and the *right* panel shows a projection of the stars that are not identified as being trapped. The fact that the *right* panel is roughly axisymmetric indicates the bar decomposition is performing adequately.

We computed the second Fourier component A_2 for all particles classified as barred and unbarred. We found that 76% of the total $m = 2$ Fourier component is in the particles classified as barred (i.e., $A_{2,\text{bar}}/A_{2,\text{tot}} \sim 0.76$). Some of this is probably coming from the $m = 4$ component (e.g., boxy orbits) being classified as unbarred, or the presence of weak spiral arms. See also Petersen et al. (2021) for more details on the orbit family breakdown.

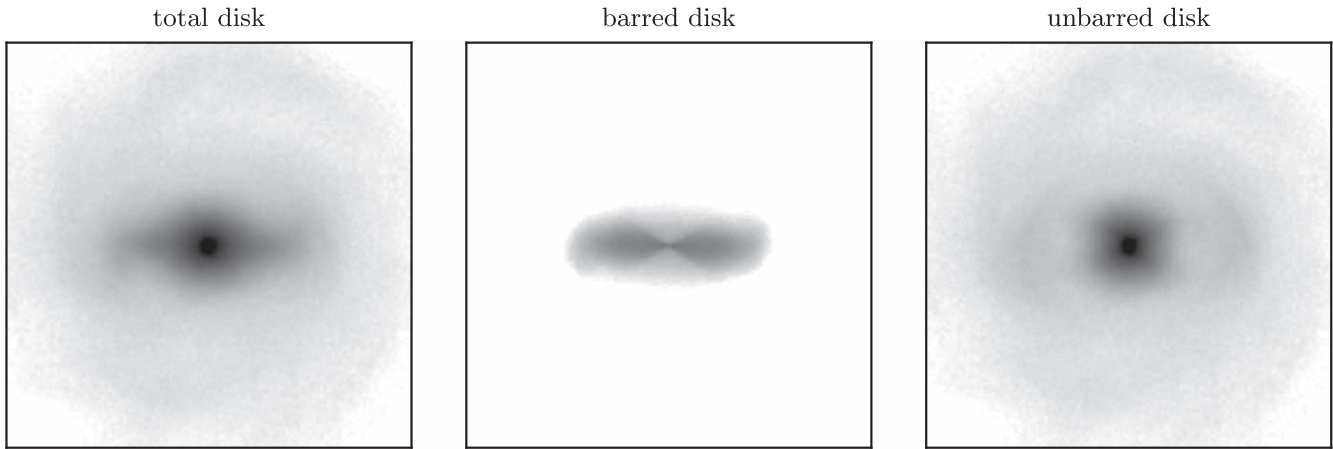


Figure 10. Disk decomposition into the barred and unbarred disk. This procedure is based on Petersen et al. (2016). The left panel shows a face-on surface density projection through the stellar component of the SMUGGLE simulation (disk and bulge) at $t = 1$ Gyr. The middle panel shows the component of the disk identified as being trapped in the bar, while the right panel shows the component of the disk identified as not being trapped in the bar. The fact that the untrapped stars form a roughly axisymmetric structure indicates our bar decomposition is sufficiently accurate. We have computed that 76% of the second Fourier component resides in the stars classified as being trapped in the bar.

Appendix B Varying Pattern Speed

When the bar slows down, we argue that this induces a larger positive torque from the gas phase. Only gas within corotation will flow inward, while gas outside corotation will flow outward (Hopkins & Quataert 2011). Since the corotation radius is larger for more slowly rotating bars, it follows that more slowly rotating bars should be more efficient at driving gas inflows and thus experience a larger positive torque from the gas phase.

We performed an experiment to test this hypothesis by freezing the stellar disk in the SMUGGLE run and forcing it to rotate at a constant angular rate. This has the effect of forcing the bar to rotate as a solid body at a constant angular rate that we control. The gas is evolved self-consistently with this rotating disk. We measured the torque on the bar by the gas phase at different rotation rates. The result of this experiment is illustrated in Figure 11, which shows that a more slowly rotating bar experiences a larger positive torque from the gas.

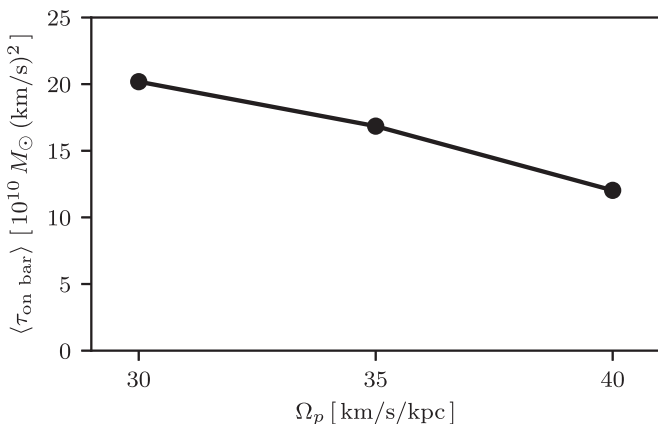


Figure 11. Average torque exerted by gas on a bar that rotates at a fixed pattern speed. Because only gas within the corotation radius is able to infall and slower bars have larger corotation radii, slower bars experience a larger net torque than faster bars. The setup of the simulations used here is identical to the SMUGGLE case discussed earlier, except the N -body disk is rotated as a solid body with a constant angular velocity.

We also note that, because Hopkins & Quataert (2011) predict gas outside of corotation will flow outward, the bar should exert a positive torque on that gas. Indeed, we measured the average torque on gas outside corotation from $t = 3$ Gyr to 5 Gyr to be 0.87 in code units ($10^{10} M_{\odot} (\text{km s}^{-1})^2$). For reference, the average torque inside corotation is -10.8 over the same time period and in the same units. So, while gas outside corotation does experience a positive torque, the total torque on the gas phase is still negative.

Appendix C Stars Instead of Gas

In the SMUGGLE model considered in this work, we instantaneously added gas to the N -body system after 1.5 Gyr of evolution. One might wonder if this sudden change to the potential is responsible for the stable pattern speed evolution. To test whether this is the case, we added mass to the system in the same way we did for the SMUGGLE model, but using collisionless particles instead of gas. The result of this experiment is shown in Figure 12. While there is an offset

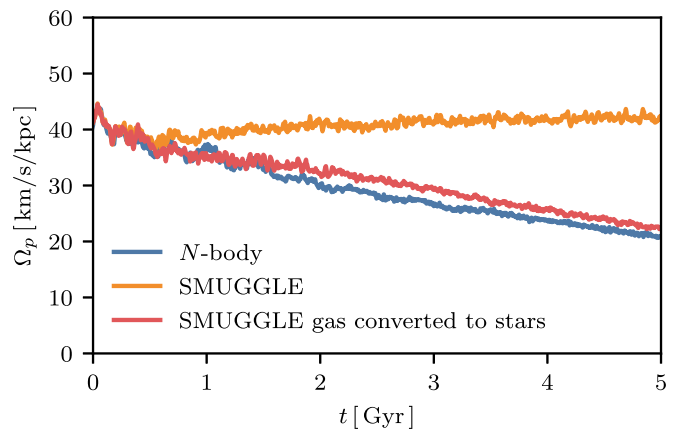


Figure 12. Pattern speed evolution of a model in which we instantaneously add stars instead of gas to the simulation, with the same density profile as the gas phase. The pattern speed evolution in this case is qualitatively similar to that of the N -body case, with a slight offset in the pattern speed. This test demonstrates that the stable pattern speed evolution in the SMUGGLE case is not simply a consequence of the change in potential imposed in our initial conditions.

compared to the pure N -body case, we see that the pattern speed evolution is broadly consistent with a declining pattern speed. This indicates that the gas phase is responsible for the stable pattern speed.

Appendix D Smooth Interstellar Medium

We performed a simulation of the same disk but with a simpler model of the interstellar medium (Springel & Hernquist 2003), closer to standard methods used in cosmological simulations of galaxy formation and described in more detail in Section 2. The result of this test is presented in Figure 13. We find that the pattern speed evolution is nearly the same in this case, and so we conclude that our result is not sensitive to the details of the model for the interstellar medium.

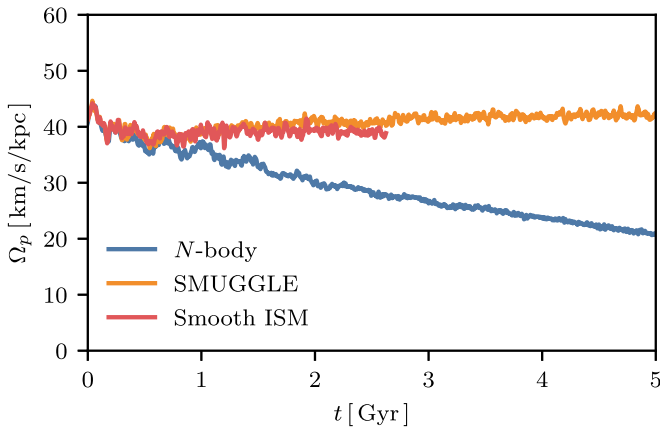


Figure 13. Pattern speed evolution of a smooth ISM model. This evolution is shown for the fiducial disk in the N -body (blue), SMUGGLE (orange), and smooth ISM (red) cases. The smooth ISM model is an older model for the ISM that treats its multiphase nature in a subgrid fashion (Springel & Hernquist 2003). This fundamentally differs from the SMUGGLE model, which explicitly resolves the hot and cold phases of the ISM (Marinacci et al. 2019). The pattern speed in the smooth ISM case is broadly similar to the evolution in the SMUGGLE case. This shows that the stability of the pattern speed is not simply a result of our assumed model for the ISM.

Appendix E Semi-analytic Model Parameters

Our semi-analytic model consisted of a three-component bar-disk-halo system. We describe here the parameters we chose for these components. The parameters of the disk and halo were chosen to match closely what we used in our fiducial simulations. The system can thus be understood as being roughly similar to the Milky Way, though no careful analysis has been performed to ensure the closest match possible.

For the dark matter halo, we used a Hernquist potential (Hernquist 1990) with mass $10^{12} M_{\odot}$ and a scale length of 26.2 kpc. For the stellar disk, we used a Miyamoto–Nagai disk (Miyamoto & Nagai 1975) with mass $4.8 \times 10^{10} M_{\odot}$, radial scale length of 2.67 kpc, and vertical scale length of 0.32 kpc. For the bar, we used the quadrupole potential described in Chiba & Schönrich (2022). We used their fiducial parameter values—specifically, we set $A = 0.02$, $b = 0.28$, and $v_c = 235 \text{ km s}^{-1}$. Our initial pattern speed is always set to $40 \text{ km s}^{-1} \text{ kpc}^{-1}$.

We integrated our model for 5 Gyr with a time step of 0.01 Gyr.

Appendix F Comparison to the Milky Way

For several Gyr, our fiducial disk exhibits several properties in reasonable agreement with the Milky Way. This is uncommon in models of galaxies that include the gas phase of the disk but no circumgalactic medium. As mentioned earlier, the pattern speed seems to match the observed pattern speed of the Milky Way’s bar (Bovy et al. 2019). Here, we briefly summarize some of the other ways our disk is comparable to the Milky Way.

We computed the circular velocity curve of our model using the AGAMA package (Vasiliev 2019). We fit the baryonic component (stellar disk, bulge, gas, and newly formed stars) with an axisymmetric cylindrical spline with 20 grid points in both the radial and vertical directions spanning 0.2–50 kpc in the radial direction and from 0.02 to 10 kpc in the vertical direction. We fit the dark matter halo using an axisymmetric multipole fit with a maximum angular harmonic coefficient of $l = 2$, to account for the compression of the halo by the disk. We plot the circular velocity curve at $t = 1$ Gyr in Figure 14 compared to observational estimates (Eilers et al. 2019). The SMUGGLE disk (which includes additional mass in the form of gas) has a slightly higher circular velocity than the N -body disk, which itself is slightly higher than the observational estimates. Overall, though, the circular velocity curves between our model and that observed in the Milky Way are broadly consistent.

We also show the evolution of the surface density profile in Figure 15. We find that, in our simulation, the atomic and molecular gas surface density and the SFR surface density are broadly consistent with the expected values for the Milky Way (Kalberla & Dedes 2008; Evans et al. 2022). The discrepancy between 1 and 4 kpc in the molecular and SFR surface density is probably due to the fact that the distances to molecular clouds that underline this work used a simple kinematic distance based on an axisymmetric model of the Milky Way (Miville-Deschênes et al. 2017), which is not accurate in the bar region where gas exhibits large noncircular velocities.

We measured the initial scale height of the atomic gas disk in a bin extending from $R = 7.5$ kpc to $R = 8.5$ kpc. The initial vertical profile is fit well by a Gaussian with a scale height of 110 pc. At $t = 1$ Gyr, the vertical profile in the same radial bin

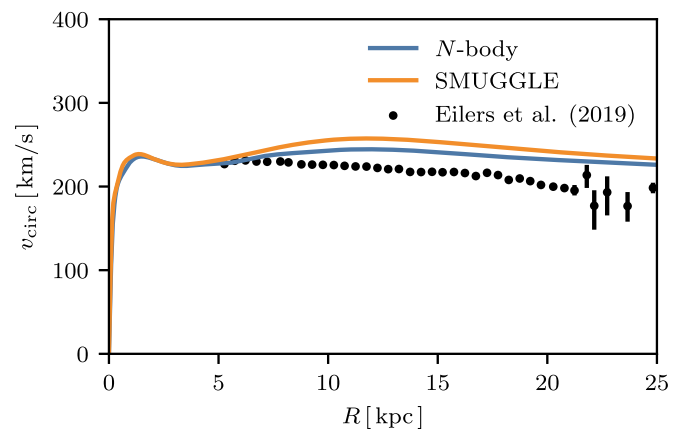


Figure 14. The circular velocity curve of our setups at $t = 1$ Gyr. This curve is shown for the N -body run (blue) and the SMUGGLE run (orange) compared to observational estimates for the Milky Way (Eilers et al. 2019). We see that the circular velocity curve for both runs is marginally larger than the Milky Way’s, but still comparable. The SMUGGLE circular velocity curve is larger than the N -body curve, due to the additional mass in the gas phase.

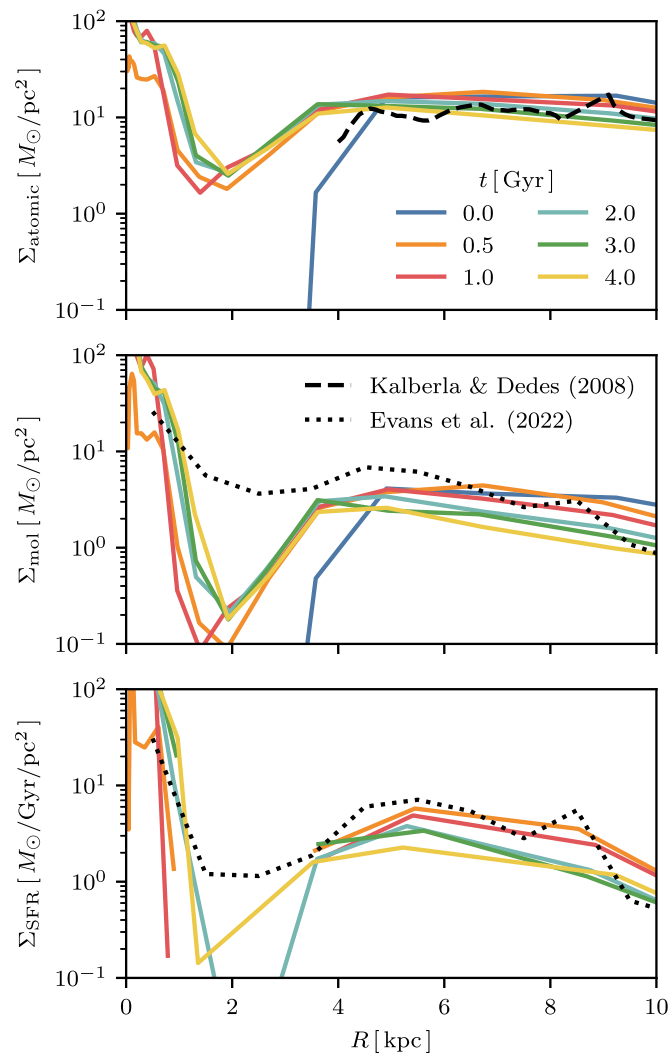



Figure 15. The time evolution of the atomic gas surface density (upper), molecular gas surface density (middle), and the star formation rate (SFR) surface density (lower) at various times during our fiducial simulation. Colored lines indicate the profiles at selected times during the simulation, the black dashed lines indicate observations for the atomic gas (Kalberla & Dedes 2008), and black dotted lines indicate a model that allows the CO-to-H₂ conversion factor X_{CO} to vary with metallicity (Evans et al. 2022). Molecular gas surface densities were provided separately (N. Evans 2023, private communication). We see that the molecular gas and SFR surface densities are within an order of magnitude of the Milky Way’s typical values at all times. We see a sharp decrease in the gas and SFR surface densities along the extent of the bar from ~ 1 to ~ 4 kpc, related to the gas inflow in this region.

is better fit by an exponential profile with scale height of 74 pc. These are somewhat lower than the observed value in the HI disk of ~ 200 pc (Malhotra 1995; Marasco et al. 2017). This may be caused by the model in our simulations not driving enough turbulent pressure, and it is an interesting avenue for further investigation.

ORCID iDs

Angus Beane  <https://orcid.org/0000-0002-8658-1453>
 Lars Hernquist  <https://orcid.org/0000-0001-6950-1629>
 Federico Marinacci  <https://orcid.org/0000-0003-3816-7028>
 Charlie Conroy  <https://orcid.org/0000-0002-1590-8551>
 Laura V. Sales  <https://orcid.org/0000-0002-3790-720X>
 Paul Torrey  <https://orcid.org/0000-0002-5653-0786>
 Mark Vogelsberger  <https://orcid.org/0000-0001-8593-7692>

References

- Aguerri, J. A. L., Méndez-Abreu, J., & Corsini, E. M. 2009, *A&A*, 495, 491
 Aguerri, J. A. L., Méndez-Abreu, J., Falcón-Barroso, J., et al. 2015, *A&A*, 576, A102
 Algorry, D. G., Navarro, J. F., Abadi, M. G., et al. 2017, *MNRAS*, 469, 1054
 Astropy Collaboration, Price-Whelan, A. M., Sipőcz, B. M., et al. 2018, *AJ*, 156, 123
 Astropy Collaboration, Robitaille, T. P., Tollerud, E. J., et al. 2013, *A&A*, 558, A33
 Athanassoula, E. 2002, *ApJL*, 569, L83
 Athanassoula, E. 2003, *MNRAS*, 341, 1179
 Athanassoula, E. 2014, *MNRAS*, 438, L81
 Athanassoula, E., Machado, R. E. G., & Rodionov, S. A. 2013, *MNRAS*, 429, 1949
 Athanassoula, E., & Misiriotis, A. 2002, *MNRAS*, 330, 35
 Athanassoula, E., Morin, S., Wozniak, H., et al. 1990, *MNRAS*, 245, 130
 Aumer, M., & Schönrich, R. 2015, *MNRAS*, 454, 3166
 Berentzen, I., Shlosman, I., Martínez-Valpuesta, I., & Heller, C. H. 2007, *ApJ*, 666, 189
 Bird, J. C., Kazantzidis, S., & Weinberg, D. H. 2012, *MNRAS*, 420, 913
 Blanton, M. R., & Moustakas, J. 2009, *ARA&A*, 47, 159
 Blitz, L., & Spergel, D. N. 1991, *ApJ*, 379, 631
 Bournaud, F., & Combes, F. 2002, *A&A*, 392, 83
 Bournaud, F., Combes, F., & Semelin, B. 2005, *MNRAS*, 364, L18
 Bovy, J., Leung, H. W., Hunt, J. A. S., et al. 2019, *MNRAS*, 490, 4740
 Bureau, M., Freeman, K. C., Pfitzner, D. W., & Meurer, G. R. 1999, *AJ*, 118, 2158
 Buttitta, C., Corsini, E. M., Aguerri, J. A. L., et al. 2023, *MNRAS*, 521, 2227
 Buttitta, C., Corsini, E. M., Cuomo, V., et al. 2022, *A&A*, 664, L10
 Chabrier, G. 2003, *PASP*, 115, 763
 Chemin, L., & Hernandez, O. 2009, *A&A*, 499, L25
 Chequers, M. H., Spekkens, K., Widrow, L. M., & Gilhuly, C. 2016, *MNRAS*, 463, 1751
 Chiba, R., Friske, J. K. S., & Schönrich, R. 2021, *MNRAS*, 500, 4710
 Chiba, R., & Schönrich, R. 2021, *MNRAS*, 505, 2412
 Chiba, R., & Schönrich, R. 2022, *MNRAS*, 513, 768
 Collier, A., Shlosman, I., & Heller, C. 2018, *MNRAS*, 476, 1331
 Collier, A., Shlosman, I., & Heller, C. 2019, *MNRAS*, 488, 5788
 Combes, F., & Sanders, R. H. 1981, *A&A*, 96, 164
 Contopoulos, G. 1980, *A&A*, 81, 198
 Corsini, E. M. 2011, *MSAIS*, 18, 23
 Crain, R. A., Schaye, J., Bower, R. G., et al. 2015, *MNRAS*, 450, 1937
 Cuomo, V., Corsini, E. M., Aguerri, J. A. L., et al. 2019, *MNRAS*, 488, 4972
 Debattista, V. P., & Sellwood, J. A. 1998, *ApJL*, 493, L5
 Debattista, V. P., & Sellwood, J. A. 2000, *ApJ*, 543, 704
 D’Onghia, E., & Aguerri, L. J. A. 2020, *ApJ*, 890, 117
 Dubinski, J., Berentzen, I., & Shlosman, I. 2009, *ApJ*, 697, 293
 Eilers, A.-C., Hogg, D. W., Rix, H.-W., & Ness, M. K. 2019, *ApJ*, 871, 120
 Eskridge, P. B., Frogel, J. A., Pogge, R. W., et al. 2000, *AJ*, 119, 536
 Evans, N. J., Kim, J.-G., & Ostriker, E. C. 2022, *ApJL*, 929, L18
 Font, J., Beckman, J. E., Martínez-Valpuesta, I., et al. 2017, *ApJ*, 835, 279
 Fragkoudi, F., Grand, R. J. J., Pakmor, R., et al. 2021, *A&A*, 650, L16
 Frankel, N., Pillepich, A., Rix, H.-W., et al. 2022, *ApJ*, 940, 61
 Fraser-McKelvie, A., Aragón-Salamanca, A., Merrifield, M., et al. 2020, *MNRAS*, 495, 4158
 Friedli, D., & Benz, W. 1993, *A&A*, 268, 65
 Garma-Oehmichen, L., Cano-Díaz, M., Hernández-Toledo, H., et al. 2020, *MNRAS*, 491, 3655
 Gavazzi, G., Consolandi, G., Dotti, M., et al. 2015, *A&A*, 580, A116
 Grand, R. J. J., Gómez, F. A., Marinacci, F., et al. 2017, *MNRAS*, 467, 179
 Guo, R., Mao, S., Athanassoula, E., et al. 2019, *MNRAS*, 482, 1733
 Guo, Y., Jogee, S., Finkelstein, S. L., et al. 2023, *ApJL*, 945, L10
 Harris, C. R., Millman, K. J., van der Walt, S. J., et al. 2020, *Natur*, 585, 357
 Hayden, M. R., Bovy, J., Holtzman, J. A., et al. 2015, *ApJ*, 808, 132
 Hernquist, L. 1990, *ApJ*, 356, 359
 Hernquist, L., & Katz, N. 1989, *ApJS*, 70, 419
 Hernquist, L., & Weinberg, M. D. 1992, *ApJ*, 400, 80
 Hohl, F. 1971, *ApJ*, 168, 343
 Hohl, F. 1976, *AJ*, 81, 30
 Holley-Bockelmann, K., Weinberg, M., & Katz, N. 2005, *MNRAS*, 363, 991
 Hopkins, P. F., & Quataert, E. 2011, *MNRAS*, 415, 1027
 Hopkins, P. F., Wetzell, A., Kereš, D., et al. 2018, *MNRAS*, 480, 800
 Hunt, J. A. S., Hong, J., Bovy, J., Kawata, D., & Grand, R. J. J. 2018, *MNRAS*, 481, 3794
 Hunter, J. D. 2007, *CSE*, 9, 90
 Johnson, H. M. 1957, *AJ*, 62, 19

- Kalberla, P. M. W., & Dedes, L. 2008, *A&A*, **487**, 951
- Lam, S. K., Pitrou, A., & Seibert, S. 2015, in SC15: The Int. Conf. for High Performance Computing, Networking, Storage and Analysis (New York: ACM), **1**
- Long, S., Shlosman, I., & Heller, C. 2014, *ApJL*, **783**, L18
- Lynden-Bell, D., & Kalnajs, A. J. 1972, *MNRAS*, **157**, 1
- Malhotra, S. 1995, *ApJ*, **448**, 138
- Marasco, A., Fraternali, F., van der Hulst, J. M., & Oosterloo, T. 2017, *A&A*, **607**, A106
- Marinacci, F., Sales, L. V., Vogelsberger, M., Torrey, P., & Springel, V. 2019, *MNRAS*, **489**, 4233
- Márquez, I., Durret, F., González Delgado, R. M., et al. 1999, *A&AS*, **140**, 1
- Martinez-Valpuesta, I., Shlosman, I., & Heller, C. 2006, *ApJ*, **637**, 214
- Menéndez-Delmestre, K., Sheth, K., Schinnerer, E., Jarrett, T. H., & Scoville, N. Z. 2007, *ApJ*, **657**, 790
- Michel-Dansac, L., & Wozniak, H. 2006, *A&A*, **452**, 97
- Miville-Deschênes, M.-A., Murray, N., & Lee, E. J. 2017, *ApJ*, **834**, 57
- Miyamoto, M., & Nagai, R. 1975, *PASJ*, **27**, 533
- Nelson, D., Pillepich, A., Springel, V., et al. 2019, *MNRAS*, **490**, 3234
- Okamoto, T., Isoe, M., & Habe, A. 2015, *PASJ*, **67**, 63
- O'Neill, J. K., & Dubinski, J. 2003, *MNRAS*, **346**, 251
- Ostriker, J. P., & Peebles, P. J. E. 1973, *ApJ*, **186**, 467
- Peschken, N., & Łokas, E. L. 2019, *MNRAS*, **483**, 2721
- Petersen, M. S., Weinberg, M. D., & Katz, N. 2016, *MNRAS*, **463**, 1952
- Petersen, M. S., Weinberg, M. D., & Katz, N. 2019a, arXiv:1903.08203
- Petersen, M. S., Weinberg, M. D., & Katz, N. 2019b, *MNRAS*, **490**, 3616
- Petersen, M. S., Weinberg, M. D., & Katz, N. 2021, *MNRAS*, **500**, 838
- Pillepich, A., Nelson, D., Springel, V., et al. 2019, *MNRAS*, **490**, 3196
- Purcell, C. W., Bullock, J. S., Tollerud, E. J., Rocha, M., & Chakrabarti, S. 2011, *Natur*, **477**, 301
- Regan, M. W., & Teuben, P. J. 2004, *ApJ*, **600**, 595
- Roshan, M., Banik, I., Ghafourian, N., et al. 2021a, *MNRAS*, **503**, 2833
- Roshan, M., Ghafourian, N., Kashfi, T., et al. 2021b, *MNRAS*, **508**, 926
- Saha, K., & Naab, T. 2013, *MNRAS*, **434**, 1287
- Savitzky, A., & Golay, M. J. E. 1964, *AnaCh*, **36**, 1627
- Schaye, J., Crain, R. A., Bower, R. G., et al. 2015, *MNRAS*, **446**, 521
- Sellwood, J. A., & Binney, J. J. 2002, *MNRAS*, **336**, 785
- Sellwood, J. A., & Debattista, V. P. 2006, *ApJ*, **639**, 868
- Sellwood, J. A., & Wilkinson, A. 1993, *RPPh*, **56**, 173
- Shlosman, I., Begelman, M. C., & Frank, J. 1990, *Natur*, **345**, 679
- Shlosman, I., Frank, J., & Begelman, M. C. 1989, *Natur*, **338**, 45
- Springel, V. 2010, *MNRAS*, **401**, 791
- Springel, V., Di Matteo, T., & Hernquist, L. 2005, *MNRAS*, **361**, 776
- Springel, V., & Hernquist, L. 2003, *MNRAS*, **339**, 289
- Tacconi, L. J., Genzel, R., & Sternberg, A. 2020, *ARA&A*, **58**, 157
- Tremaine, S., & Weinberg, M. D. 1984a, *ApJL*, **282**, L5
- Tremaine, S., & Weinberg, M. D. 1984b, *MNRAS*, **209**, 729
- Valenzuela, O., & Klypin, A. 2003, *MNRAS*, **345**, 406
- Vasiliev, E. 2019, *MNRAS*, **482**, 1525
- Villa-Vargas, J., Shlosman, I., & Heller, C. 2009, *ApJ*, **707**, 218
- Villa-Vargas, J., Shlosman, I., & Heller, C. 2010, *ApJ*, **719**, 1470
- Virtanen, P., Gommers, R., Oliphant, T. E., et al. 2020, *NatMe*, **17**, 261
- Vogelsberger, M., Genel, S., Springel, V., et al. 2014a, *Natur*, **509**, 177
- Vogelsberger, M., Genel, S., Springel, V., et al. 2014b, *MNRAS*, **444**, 1518
- Vogelsberger, M., Marinacci, F., Torrey, P., & Puchwein, E. 2020, *NatRP*, **2**, 42
- Weinberg, M. D. 1985, *MNRAS*, **213**, 451
- Weinberg, M. D., & Katz, N. 2007, *MNRAS*, **375**, 460
- Weinberger, R., Springel, V., & Pakmor, R. 2020, *ApJS*, **248**, 32
- Werk, J. K., Putman, M. E., Meurer, G. R., et al. 2010, *ApJ*, **715**, 656
- Whitaker, K. E., Williams, C. C., Mowla, L., et al. 2021, *Natur*, **597**, 485